Modeling programmable drug delivery in bioelectronics with electrochemical actuation

Raudel Avila[a], Chenhang Li[a,1], Yeguang Xue[a,1], John A. Rogers[a,b,c,d,e,f,g], and Yonggang Huang[a,b,c,h,2]

[a]Department of Mechanical Engineering, Northwestern University, Evanston, IL 60208; [b]Querrey Simpson Institute for Bioelectronics, Northwestern University, Evanston, IL 60208; [c]Department of Materials Science and Engineering, Northwestern University, Evanston, IL 60208; [d]Department of Biomedical Engineering, Northwestern University, Evanston, IL 60208; [e]Department of Electrical and Computer Engineering, Northwestern University, Evanston, IL 60208; [f]Department of Chemistry, Northwestern University, Evanston, IL 60208; [g]Department of Neurological Surgery, Feinberg School of Medicine, Northwestern University, Chicago, IL 60611; and [h]Department of Civil and Environmental Engineering, Northwestern University, Evanston, IL 60208

Drug delivery systems featuring electrochemical actuation represent an emerging class of biomedical technology with programmable volume/flowrate capabilities for localized delivery. Recent work establishes applications in neuroscience experiments involving small animals in the context of pharmacological response. However, for programmable delivery, the available flowrate control and delivery time models fail to consider key variables of the drug delivery system—microfluidic resistance and membrane stiffness. Here we establish an analytical model that accounts for the missing variables and provides a scalable understanding of each variable influence in the physics of delivery process (i.e., maximum flowrate, delivery time). This analytical model accounts for the key parameters—initial environmental pressure, initial volume, microfluidic resistance, flexible membrane, current, and temperature—to control the delivery and bypasses numerical simulations allowing faster system optimization for different in vivo experiments. We show that the delivery process is controlled by three nondimensional parameters, and the volume/flowrate results from the proposed analytical model agree with the numerical results and experiments. These results have relevance to the many emerging applications of programmable delivery in clinical studies within the neuroscience and broader biomedical communities.

drug delivery | electrochemical actuation | flexible membrane | mechanics | analytical model

Drug delivery techniques for treatment, cure, diagnosis, and prevention of illnesses have substantially evolved from systemic absorption of pharmacological agents through tissue membranes to localized drug release in regions of interest (1). Modern drug delivery methods help researchers study the effects of a medication intended for a specific body region while decreasing the potential side effects from unwanted interactions in other body regions (2). In drug delivery, the effect of pharmacological ingredients, drug amount, target regions, delivery rates, and dosage time, varies between delivery approaches (1, 3) ranging from ubiquitous ingestible tablets/capsules to injectable microsystems.

The growing opportunities in localized delivery and clinical research motivated the development of microsystems for volume and flowrate control (4–10) in pharmacological experiments involving small animals (11–18). Design of implantable microsystems requires compact size, power consumption, and biocompatible material considerations (19) that vary between actuation methods (e.g., magnetic, thermal, optical, mechanical, or electrochemical) to deliver the drug without complications (9). A biocompatible encapsulation limits any negative effects derived from implantation or during continuous operation while in proximity with surrounding tissues/fluids. Excessive thermal heating and high-power consumption can 1) affect animal behavior and damage the implanted region and 2) require bulk electronics (i.e., battery) that increase the size and overall weight of the microsystem.

In implantable delivery systems, electrochemical actuation offers 1) low power consumption, 2) negligible heat generation, 3) reconfigurable volume sizes (e.g., small or large drug reservoirs), 4) higher flowrates and fast response time (9, 20), 5) simplified implantation and unrestricted movement of animals for in vivo studies, and in some cases 6) refillable (7, 15, 16, 21) for repeated studies. Wireless electrochemical actuation features an inductive link to harvest the electrical current applied to a set of interdigitated electrodes in contact with an electrolyte solution and initiate the chemical reaction (22–26). Continuous gas formation (i.e., hydrogen H_2 and oxygen O_2) gradually increases the pressure inside the electrolyte reservoir to deform a flexible polymer membrane (15, 16, 22, 27) pushing the drug via partially implanted microchannels to the target region inside the animal. Fig. 1 illustrates the schematics of an electrochemical pump. Electrochemical actuation systems have been used to target localized delivery of insulin (28), cancer agents (29, 30), hormone (31) and intraocular (21) drug delivery, as well as therapeutic drug studies (4, 32).

In 2019, a wireless, battery-free, and refillable electrochemical microsystem combined optogenetic and pharmacological stimulation in a single experiment with programmable flowrates and unrestricted animal movement (15, 16). These miniaturized injectable devices overcome the limitations of supplementary hardware required in combined stimulation and offer compatible

Significance

Drug delivery systems with electrochemical actuation offer programmable volume/flowrates in miniaturized form factors for in vivo pharmacological experiments in freely moving animals where flowrate control and delivery time are important. Here, we present an analytical model that accounts for all the problem variables influencing the drug delivery in nondimensional parameters for pressure, volume, and microfluidic channels. Variation of the nondimensional parameters provides a scalable relationship for the volume/flowrate and delivery time. This analytical model agrees well with experiments and gives researchers additional parameters when designing a programmable drug delivery system for neuroscience/clinical research.

ENGINEERING

Fig. 1. Schematic diagram of the electrochemical micropump system. (*A*) Before, (*B*) during, and (*C*) after the drug delivery process highlighting the relevant volume, pressure, and microchannel parameters in the drug delivery process.

form factors for large-scale manufacturing, making it a suitable option for widespread use in animal behavioral studies (31, 33, 34) where accurate control of volume and flowrate are critical. Programmed drug delivery influences the pharmacodynamic response in the animals (31) and excessively high or low rates can damage neighboring tissues or block the microfluidic channels (15), respectively. To predict the fluid delivery rates, a linear relationship between the effective current and flowrate has been used in the past (35, 36). However, this model neglects the microfluidic resistance and flexible membrane mechanics and overestimates the flowrate (15). Recently, a numerical model, derived from the rate form of the ideal gas law, was proposed and it accounts for the 1) microfluidic cross-sectional area and length, and 2) flexible membrane elasticity (16). Still, the model requires extensive numerical simulations to predict volume and flowrates, and it is difficult to find time-scaling relationships for drug delivery.

Here, we develop an analytical model that gives an accurate relation between the current and flowrate and offers a simple analytical solution of the drug delivery process, while considering all important factors in the microsystem design, including microchannel and flexible membrane which are difficult to

account for in prior studies, without the need for numerical simulations. The flexible membrane effects were derived from mechanics theory for an arbitrary flexible polymer and used in the volume and flowrate calculations. Motivated by the ongoing adoption of implantable electrochemical microsystems in drug delivery, the analytical model described in the following identifies the key parameters that control the volume and flowrate during the drug delivery and gives researchers much larger design space (e.g., geometrical, flexural, and fluidic) for electrochemical microsystems in future clinical studies. This article presents results from experiments and previous numerical models to validate the proposed theory.

Results and Discussion

Modeling of Drug Delivery. Fig. 1 illustrates the drug delivery process using electrochemical actuation where electrical current i in the interdigitated electrodes initiates (Fig. 1*A*) a chemical reaction that increases the pressure P inside the electrolyte reservoir due to gas formation. The buildup pressure continuously deforms the flat flexible polymer membrane (Fig. 1*B*) into a spherical cap and pushes the drug out of the reservoir through a network of microfluidic channels and into the target delivery

region (Fig. 1C). For electrochemical actuation devices, the drug delivery process can be derived from the ideal gas law $P(V + V_0) = nRT$ by writing the rate form as

$$\dot{P}(V + V_0) + P\dot{V} = \dot{n}RT, \qquad [1]$$

where P is the pressure, V_0 and V are the initial gas volume and volume change inside the electrolyte reservoir, respectively, $\dot{n} = \frac{3i}{4F}$ is the gas generation rate related to the effective current i, F is the Faraday constant, R is the ideal gas constant, and T is the temperature. The force equilibrium gives

$$P = \frac{12\mu L\dot{V}}{ab^3\left(1 - 0.63\frac{b}{a}\right)} + f(V) + P_0, \qquad [2]$$

where the first term $\frac{12\mu L\dot{V}}{ab^3\left(1 - 0.63\frac{b}{a}\right)}$ represents the microfluidic resistance (37, 38) for a rectangular cross-section, a, b, and L are the width, height, and length of the delivery channel (Fig. 1), respectively, and μ is the viscosity of the drug (valid for $b < a$, for a square cross-section it simplifies $\sim\frac{32\mu L\dot{V}}{a^4}$); the second term $f(V)$ is the pressure needed to deform the flexible membrane leading to the volume change V inside the electrolyte reservoir, and this pressure–volume relationship $f(V)$ of the flexible membrane could be determined numerically by the finite-element analysis (FEA) as in prior studies, but now completely analytical as discussed later in this paper; and the third term P_0 is the initial environmental pressure. Substituting the gas generation rate and pressure into Eq. **1** yields a second-order ordinary-differential equation (ODE) of the form

$$\left[\frac{32\mu L}{a^4}\ddot{V} + f'(V)\dot{V}\right](V + V_0) + \left[\frac{32\mu L}{a^4}\dot{V} + f(V) + P_0\right]\dot{V} = \frac{3iRT}{4F}, \qquad [3]$$

that describes the drug delivery process with square cross-section microfluidic channels. Eq. **3** was solved numerically (15, 16) with the initial conditions $V(t = 0) = 0$, and $\dot{V}(t = 0) = 0$ to determine the delivered drug volume and flowrate versus time. The numerical solution of Eq. **3**, while very useful, fails to provide a scalable understanding of each parameter in the drug delivery.

The following nondimensional variables and parameters are introduced: normalizing pressure terms P, $f(V)$ and P_0 by the ratio $\frac{Eh}{R_0}$, where E, h, and R_0 are the flexible membrane Young modulus, thickness, and radius, respectively; normalizing the volume terms by R_0^3, i.e., $V_0^* = \frac{V_0}{R_0^3}$ and $V^* = \frac{V}{R_0^3}$; rewriting the function $f(V)$ by a normalized function $\frac{Eh}{R_0}G\left(\frac{V}{R_0^3}\right)$, where G is a nondimensional function; and introducing a nondimensional time of the form $t^* = \frac{3iRT}{4FEhR_0^2}t$. All the relationships with the nondimensional parameters are given in *SI Appendix*, Table S1. Eq. **3** can then be rewritten nondimensionally as

$$\left[M^*\frac{d^2V^*}{dt^{*2}} + G'(V^*)\frac{dV^*}{dt^*}\right](V^* + V_0^*)$$
$$+ \left[M^*\frac{dV^*}{dt^*} + G(V^*) + P_0^*\right]\frac{dV^*}{dt^*} = 1, \qquad [4]$$

where the nondimensional parameter $M^* = \frac{24\mu L}{a^4}\frac{iRTR_0^2}{Fh^2E^2}$ represents the microfluidic resistance and it combines the effects of microfluid channel (a and L), drug (μ), flexible membrane (E, h, and R_0), current (i), and temperature (T); and $V_0^* = \frac{V_0}{R_0^3}$, and $P_0^* = \frac{P_0R_0}{Eh}$ represent the initial volume and initial environmental pressure, respectively. These three nondimensional parameters control the

drug delivery process (*SI Appendix*, Supplementary Note 1). We integrate Eq. **4** to yield the following first-order ODE for V^*:

$$(V^* + V_0^*)\left[M^*\frac{dV^*}{dt^*} + G(V^*)\right] + V^*P_0^* - t^* = 0, \qquad [5]$$

with the initial conditions $V^*(t^* = 0) = 0$.

For vanishingly small M^*, i.e., negligible microfluidic resistance, the equation above is simplified to the following:

$$t^* = (V^* + V_0^*)G(V^*) + V^*P_0^*, \qquad [6]$$

which gives the normalized time in terms of the normalized drug volume (and initial environmental pressure P_0^* and initial volume V_0^*). It is useful to estimate the drug delivery time $t_{delivery}$ for a given drug volume V, and $t_{delivery}$ is linear with respect to V_0^* and P_0^*. Its inverse, i.e., the drug volume versus time, is denoted by $V_{SOL}^*(t^*)$, which is the solution of Eq. **5** at the limit $M^* = 0$, although it does not satisfy the initial condition $\dot{V}(t = 0) = 0$.

For small but nonvanishing M^* (i.e., accounting for the microfluidic resistance), Eq. **5** is solved by the singular perturbation method (*SI Appendix*, Supplementary Note 2) as

$$V^* = V_{SOL}^*(t^*) - \frac{M^*}{V_0^*\left(\frac{64h^2}{3\pi R_0^2} + \frac{P_0^*}{V_0^*}\right)^2}\left[1 - e^{-\left(\frac{64h^2}{3\pi R_0^2} + \frac{P_0^*}{V_0^*}\right)\frac{t^*}{M^*}}\right], \qquad [7]$$
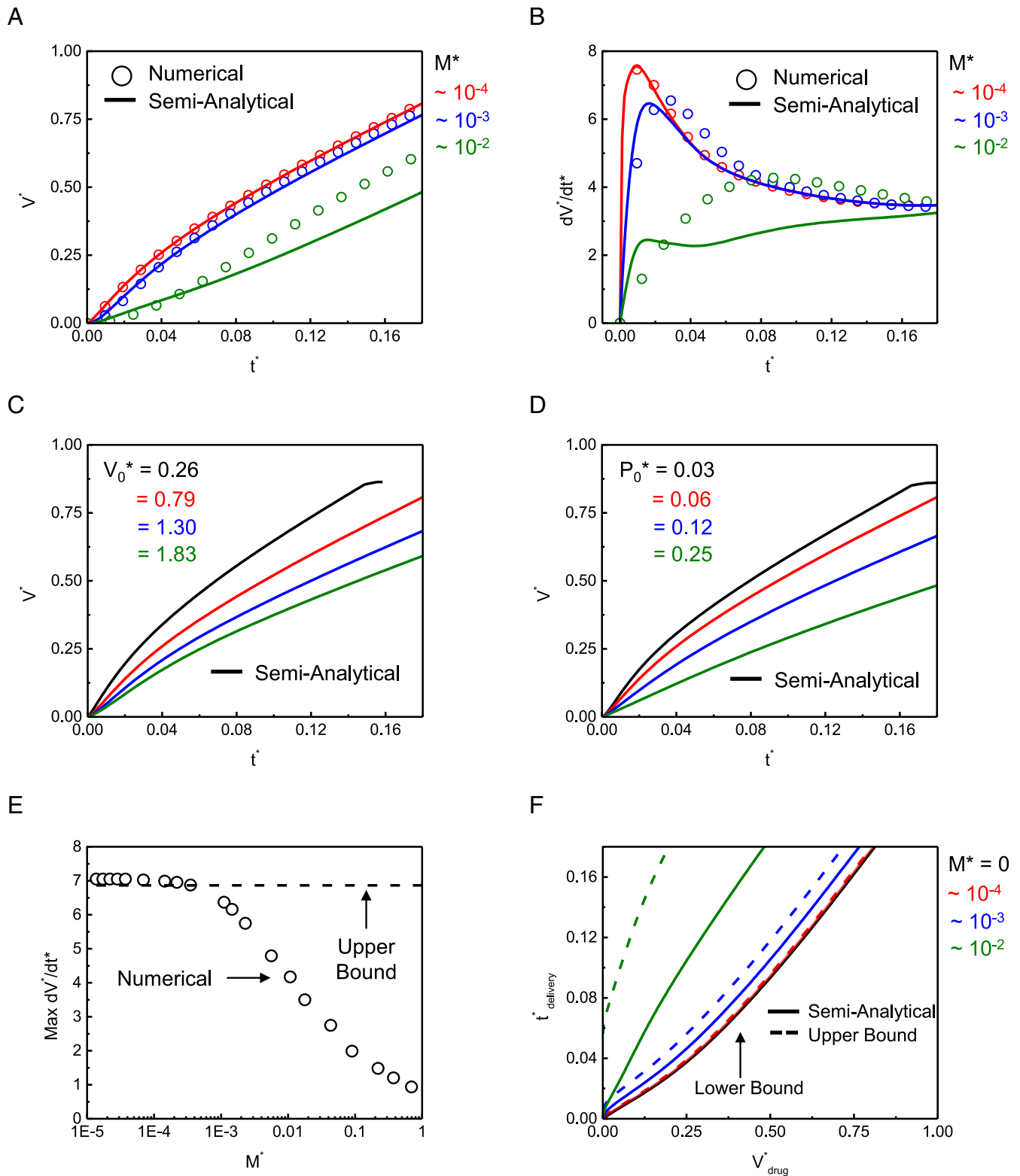
where the first term on the right-hand side is the solution of Eq. **6**, the second term decays exponentially with time, and together they satisfy the initial condition $\dot{V}(t = 0) = 0$.

Fig. 2 *A* and *B* show the results in Eq. **5** (numerical solution) and Eq. **7** [semianalytical model with function $f(V)$ still determined from FEA]* when M^* changes for the base line values $V_0^* = 0.79$, $P_0^* = 0.06$, and $\frac{h}{R_0} = \frac{1}{8}$ obtained from the experiments. For both volume V^* and flowrate $\frac{dV^*}{dt^*}$, the numerical solution and semianalytical model agree very well for values of $M^* \sim 10^{-4}$ and $\sim 10^{-3}$, though the results deviate at $M^* \sim 10^{-2}$ because M^* is no longer small (assumption in Eq. **7**). The volume V^* decreases as the microfluidic resistance M^* increases (Fig. 2A). It also decreases as the initial volume V_0^* increases (Fig. 2C) because, for small V_0^*, the PV term quickly overwhelms the initial volume term PV_0 resulting in a faster volume increase with time. On the contrary, for large V_0^*, the term PV_0 dominates for a substantial time, taking longer for the term PV to outperform it over time slowing down the volume increase. Similarly, the volume V^* decreases as the initial environmental P_0^* increases (Fig. 2D) because, for small P_0^*, the change in pressure due to microfluidic channel $\frac{32\mu L\dot{V}}{a^4}$ and flexible membrane deformation $f(V)$ quickly overcomes the environmental pressure P_0 for a faster volume increase; for large P_0 (e.g., drug delivery at different organ/tissues), the pressure increments due to $\frac{32\mu L\dot{V}}{a^4}$ and $f(V)$ are insignificant as compared to the initial environmental pressure slowing down the drug volume delivery.

The nondimensional maximum flowrate $\frac{dV^*}{dt^*}$, which is the peak value in Fig. 2B, is important in drug delivery. Fig. 2E reveals that the maximum flowrate $\frac{dV^*}{dt^*}$ remains relatively constant for small microfluidic resistance $M^* < 10^{-4}$ and monotonically decreases as M^* increases from 10^{-4} to 1, therefore providing a parameter to control the maximum flowrate. In addition, the

---

*The analytic expression of $f(V)$ for any polymer membrane is given later in the paper and the corresponding solution is called the analytical model, to distinguish from the semianalytical model in which $f(V)$ is obtained from FEA.

Avila et al.
Modeling programmable drug delivery in bioelectronics with electrochemical actuation

PNAS | 3 of 8
https://doi.org/10.1073/pnas.2026405118

ENGINEERING

Fig. 2. Drug delivery models and scaling results. (*A*) Numerical and semianalytical model results for normalized drug volume delivery and (*B*) normalized flowrate over normalized time for different M^*. Normalized drug volume delivery for different (*C*) initial volume V_0^* and (*D*) initial environmental pressure P_0^*. (*E*) Maximum normalized flowrate and the upper bound as a function of M^* in the numerical model. (*F*) Critical normalized time to deliver normalized drug volume for different M^*; the lower bound corresponds to $M^* = 0$. In the semianalytical model, the term $f(V)$ is obtained from FEA.

upper-bound maximum (dimensional) flowrate is derived analytically as (*SI Appendix*, Supplementary Note 3)

$$\dot{V}_{max} = \frac{3iRT}{4F\left[\frac{16Eh^3V_0}{\pi R_0^6(1-v^2)} + P_0\right]},$$ [8]

which is linearly proportional to the current i and temperature T and decreases as the initial environmental pressure P_0 or the product $\frac{Eh^3V_0}{R_0^6(1-v^2)}$ of initial volume and bending stiffness of the flexible membrane increases, where v is the Poisson ratio of the membrane. This upper-bound solution is independent of the material constitutive model, accurate for small M^*, and overestimates as M^* increases. Fig. 2*F* shows the critical nondimensional time $t^*_{delivery}$ required to deliver a nondimensional volume V^*_{drug} of drug as M^* increases. For $M^* = 0$, the solution simplifies to Eq. **6**, which becomes the lower bound (black line) as there is no microfluidic resistance. As M^* increases, the time to deliver the drug also increases, and its upper-bound estimate is given analytically (*SI Appendix*, Supplementary Note 3) by

$$t^*_{delivery} = \left\{\left[V^* + \frac{M^*}{V_0^*\left(\frac{64h^2}{3\pi R_0^2} + \frac{P_0^*}{V_0^*}\right)^2}\right] + V_0^*\right\}\frac{R_0}{Eh}f\left\{\left[V^* \right.\right.$$
$$\left.\left. + \frac{M^*}{V_0^*\left(\frac{64h^2}{3\pi R_0^2} + \frac{P_0^*}{V_0^*}\right)^2}\right]R_0^3\right\} + P_0^*\left[V^* + \frac{M^*}{V_0^*\left(\frac{64h^2}{3\pi R_0^2} + \frac{P_0^*}{V_0^*}\right)^2}\right],. \quad [9]$$

where the term $f(V)$ depends on the material's constitutive model. The semianalytical solution in Eq. **7** is clearly between the lower- and upper-bound estimate (Fig. 2*F*) and the $f(V)$ in Eq. **9** was determined from FEA using the Marlow hyperelastic constitutive model based on the stress–strain relationship of the flexible membrane in *SI Appendix*, Fig. S2.

In animal behavioral studies involving drug delivery, the precise control of flowrate is critical to avoid tissue damage in the surrounding areas caused by high flowrates and this can be achieved by adjusting the current in the experiment (15, 16). Fig. 3*A* shows that the upper bound and the numerical results of the maximum flowrate, which agree very well with the experiments [Zhang et al. (15)] for small current (< 0.3 mA), and they deviate at larger currents (> 0.3 mA) due to increasing bubble formation near the electrodes reducing the contact area between the electrodes and electrolyte solution. The top x axis of Fig. 3*A* shows the equivalent M^* for the effective current values. In the delivery presented in Fig. 3*B* (16) where $i = 0.3$ mA, the flowrate rapidly increases and reaches the maximum flowrate ~1.5 µL/min within a few seconds. This is also confirmed by the numerical results as well as the semianalytical model, which agree well with the experiments [Zhang et al. (16)]. The upper-bound solution is also shown in Fig. 3*B*, which overestimates the maximum flowrate by ~5%. The parameters used in the analytical and numerical models for Fig. 3 are listed in *SI Appendix*, Table S2.

The delivery requirements can vary between slow or instant stimulation depending on the type of biomedical experiment and target locations inside the animal body. Programmable control over the flowrate and total delivery time are critical in many neuroscience experiments to avoid any damage to the surrounding locations and ensure that the stimulation was completed within a required timeframe. Depending on the type of stimulation, the system can be designed using the three nondimensional parameters proposed in the analytical model for programmable operation of flowrates/timescales range prior to fabrication of the physical device. During the delivery, the nondimensional parameters serve as the programmable controls to

adjust flowrates and delivery timescale by adjusting parameters like the effective current depending on the experimental requirements (e.g., low flowrates preferred in the brain to avoid damage, and high flowrates to quickly suppress/reverse side effects).

Volume–Pressure Relationships. The semianalytical model presented in Eq. **7** requires FEA to determine the function $f(V)$ related to the stiffness of the flexible membrane. Fig. 4*A* shows the deformed profile of the flexible membrane obtained by FEA. The profile shows zero slope at the clamped edges under small pressure, suggesting the bending-dominated deformation. For large pressure, however, this zero slope becomes invisible, suggesting the stretching-dominated deformation. The analytical solutions of $f(V)$ are obtained in the following for different constitutive models of polymers, including linear elastic, Mooney Rivlin (39), and Marlow (40) hyperelastic models, where the last one can fit any stress–strain curve of polymers (41):

1) Bending solution (i.e., bending-dominated deformation): Under small pressure the deformation is linear elastic (and all hyperelastic models degenerate to linear elasticity). The flexible membrane can be modeled as a clamped, elastic thin plate with bending stiffness $\frac{Eh^3}{12(1-v^2)}$ (42). The volume V of the deformed membrane is linearly proportional to the pressure P, and this $P{\sim}V$ relation (42) gives

$$f(V) = \frac{16Eh^3}{\pi R_0^6(1-v^2)}V. \quad [10]$$

2) Linear elastic membrane solution (i.e., stretching-dominated deformation): Under large pressure the deformation is stretching-dominated, i.e., the bending deformation becomes negligible. For a linear elastic polymer, the equibiaxial tensile stiffness $\frac{Eh}{1-v}$ replaces the bending stiffness $\frac{Eh^3}{12(1-v^2)}$ in the analysis, which yields the following nonlinear $P{\sim}V$ relation (due to large deformation) *SI Appendix*, Supplementary Note 4:

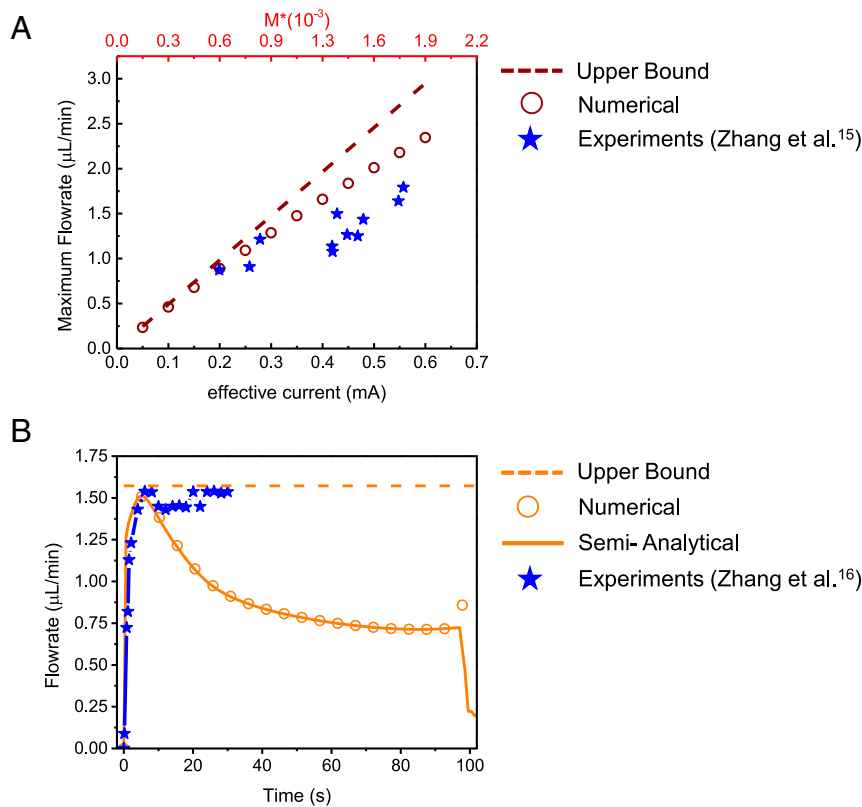$$f(V) = \frac{64Eh}{3\pi^3 R_0^{10}(1-v)}V^3. \quad [11]$$

Fig. 4*B* shows that, without any parameter fitting, the bending and linear elastic membrane solutions in the two equations above agree well with the FEA results at small and large deformation, respectively.

3) Mooney Rivlin membrane solution (i.e., stretching-dominated deformation): Under large pressure the Mooney Rivlin hyperelastic model might be more suitable for a linear elastic one. *SI Appendix*, Supplementary Note 4 gives the following $P{\sim}V$ relation in the form of parametric equations

$$f(V) = \frac{4Eh}{3R_0}\frac{\sin^3\phi}{\phi^2}\left\{\frac{2}{5}\left[\left(\frac{\phi}{\sin\phi}\right)^2 - \left(\frac{\sin\phi}{\phi}\right)^4\right] - \frac{1}{10}\left[\left(\frac{\sin\phi}{\phi}\right)^2\right.\right.$$
$$\left.\left. - \left(\frac{\phi}{\sin\phi}\right)^4\right]\right\}, \quad [12]$$

$$V = \frac{\pi R_0^3}{6}\frac{1-\cos\phi}{\sin\phi}\left[3 + \left(\frac{1-\cos\phi}{\sin\phi}\right)^2\right], \quad [13]$$

where the variable ϕ in the parametric equations above is defined in *SI Appendix*, Supplementary Note 4. Fig. 4*C* shows that the membrane solution above agrees very well with the FEA results without any parameter fitting, except for very small volume where the bending solution in Eq. **10** is more accurate.

Avila et al.
Modeling programmable drug delivery in bioelectronics with electrochemical actuation

PNAS | 5 of 8
https://doi.org/10.1073/pnas.2026405118

Fig. 3. Drug delivery experiments and modeling. (*A*) Maximum flowrate as a function of effective current for the upper-bound solution (wine dashed line), numerical (wine circles), and experimental data in Zhang et al. (15) (blue stars) for a system with microchannel cross-section 30 μm × 30 μm. (*B*) Flowrate as a function of time models for the upper-bound solution (orange dashed line), numerical (orange circles), semianalytical model (orange continuous line), and experimental data in Zhang et al. (16) (blue stars) for a system with microchannel cross-section 60 μm × 60 μm.

4) Marlow membrane solution (i.e., stretching-dominated deformation): The Marlow hyperelastic model can fit any uniaxial stress–strain curve (*SI Appendix*, Fig. S2) to the desired accuracy (41), including that of the SBS (Polystyrene-Block-Polybutadiene-Block-Polystyrene-SBS) flexible membrane used in implantable microsystems due to its soft modulus, and water/oxygen/hydrogen permeability properties (15, 16). For the Marlow hyperelastic model, the volume is still given by Eq. **13**, but the pressure becomes (*SI Appendix*, Supplementary Note 4)

$$f(V) = \frac{2h}{R_0} \frac{\sin^3 \phi}{\phi^2} \sigma_{11}(\phi), \qquad [14]$$

where the function σ_{11} is a principal stress, and it depends on the uniaxial stress–strain curve of the polymer (see *SI Appendix*, Supplementary Note 4 for details). Fig. 4*D* shows that, for SBS, the membrane solution in Eqs. **13** and **14** agrees reasonably well with the FEA results.

The analytic formula of $f(V)$ given above, combined with Eq. **7** or Eq. **9** for drug delivery time (Eq. **8** for the upper bound of maximum flowrate), is very useful to estimate the drug delivery time and the maximum flowrate analytically [i.e., it requires neither FEA for $f(V)$ nor numerical solution of ODE. Fig. 4*E* shows the analytical results of the nondimensional volume delivery over nondimensional time for SBS used in experiments (15, 16) and in Fig. 4*D*. The bending solution in Eq. **10** and the parametric membrane solution in Eqs. **12** and **13** are used as input for $f(V)$ in the analytical model in Eq. **7**, and they agree very well with the full numerical results (FEA + ODE) for small

and large volumes, respectively. This provides a simple but accurate way to estimate the drug delivery time. Similarly, Fig. 4*F* shows that the flowrate over time from the membrane solution based on the Marlow model agrees reasonably well with the full numerical results; therefore, its analytic expression can be used to estimate the flowrate in drug delivery. The analytical model [with the analytic expression of $f(V)$ without FEA] shows very good agreement with the upper-bound solution for the maximum flowrate for small M^* (*SI Appendix*, Fig. S4*A*) and is clearly between the lower- and upper-bound estimate for the critical delivery time (*SI Appendix*, Fig. S4*B*). It is important to note that the agreement between the numerical and membrane solution is dependent on the microfluidic resistance M^*, and this agreement becomes worse for large M^*.

Conclusions. In summary, this work presents an analytical model to accurately describe the drug delivery process, with a focus on electrochemical microsystems with flexible membranes. Analytical modeling, performed in a manner that includes the effects of microfluidic and flexible membrane resistance ignored in previous models, quantitatively reproduces the numerical results and experimental measurements. The results show that the simple analytical model can be used to determine the drug delivery time and maximum flowrate in large and small microsystems. These conclusions and the detailed analysis are important for the emerging applications of microsystems, with electrochemical actuation, in drug delivery studies.

Materials and Methods

FEA of Flexible Membrane Deformation. ABAQUS, a commercial FEA software, was used to model the flexible membrane deformation and calculate the
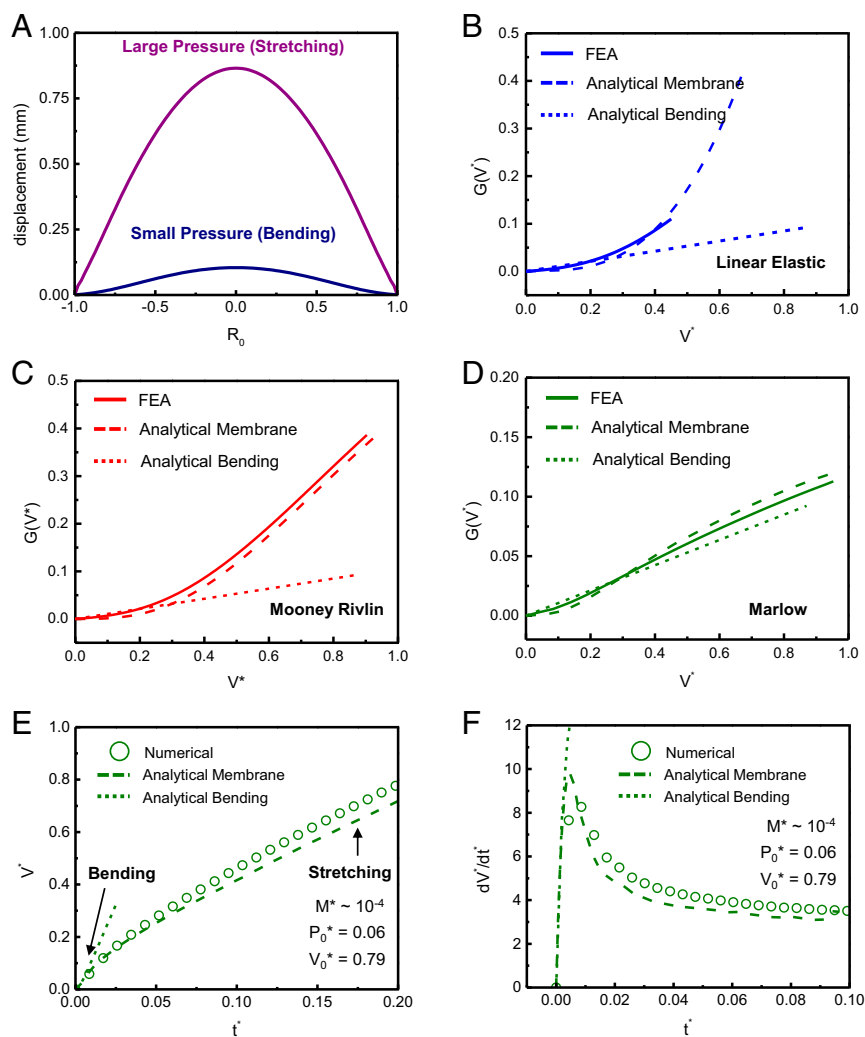
Fig. 4. Flexible membrane deformation mechanics. (*A*) FEA results of membrane displacement (bending-dominated and stretching-dominated) as a function of the membrane radius. (*B*) Nondimensional function $G(V^*)$ as a function of V^* between FEA (solid line), membrane solution (dashed line), and bending solution (dotted line) for a linear elastic material, (*C*) Mooney Rivlin hyperelastic material, and (*D*) Marlow hyperelastic material. (*E*) Nondimensional volume and (*F*) nondimensional flowrate as a function of nondimensional time for the Marlow hyperelastic material in (*D*) with different $G(V^*)$ solutions for the baseline nondimensional parameters. The analytical model uses the analytic expression of $f(V)$ determined for the different material models.

function $f(V)$. The circular flexible membrane, fixed at the circumference, is subjected to a pressure P at the bottom surface that deforms the membrane into a spherical cap shaped determined by the stiff drug reservoir shown in Fig. 1. The contact between the flexible membrane and the drug reservoir is considered in the simulation. The flexible membrane SBS and drug reservoir (Cyclic Olefin Polymer, COP) were modeled by hexahedron elements (C3D8R). The number of elements in the model was ~1×10^5, and the minimal element size was 1/6 of the thickness of the flexible membrane (150 μm). Mesh convergence of the simulation was ensured for all cases. For the linear elastic model, the membrane elastic modulus (E) and Poisson's ratio (v) are E_{SBS} = 13 MPa and v_{SBS} =0.49 for copper; in the Mooney Rivlin hyperelastic model the membrane coefficients are C_{10} = 1.744 MPa, C_{01} = 0.4362 MPa, and D_1 = 0.00923 MPa^{-1}; in the Marlow hyperelastic model uniaxial test data (*SI Appendix*, Fig. S2) were the input source to define the nominal

stress–strain curve of the SBS flexible membrane. In all cases, the elastic modulus (E) and Poisson's ratio (v) of COP are E_{COP} = 2.5 GPa and v_{COP} =0.37.

Numerical Model for Drug Delivery. MATLAB numerical solver *ode45* was used to solve Eq. **3** with the initial conditions $V(t = 0) = 0$, and $\dot{V}(t = 0) = 0$. The maximum time step was set as 1/1,000th of the total time. The $f(V)$ was obtained from FEA. All the parameters used in the numerical model are provided in *SI Appendix*, Table S2.

Data Availability. All study data are included in the article and/or *SI Appendix*.

1. D. A. Ballington, R. J. Anderson, *Pharmacy Practice for Technicians* (Paradigm Publishing, 2007).
2. G. Tiwari *et al*., Drug delivery systems: An updated review. *Int. J. Pharm. Investig.* **2**, 2–11 (2012).
3. K. Park, Controlled drug delivery systems: Past forward and future back. *J. Control. Release* **190**, 3–8 (2014).
4. A. Cobo, R. Sheybani, E. Meng, MEMS: Enabled drug delivery systems. *Adv. Healthc. Mater.* **4**, 969–982 (2015).
5. E. Meng, T. Hoang, MEMS-enabled implantable drug infusion pumps for laboratory animal research, preclinical, and clinical applications. *Adv. Drug Deliv. Rev.* **64**, 1628–1638 (2012).
6. A. C. Richards Grayson, R. Scheidt Shawgo, Y. Li, M. J. Cima, Electronic MEMS for triggered delivery. *Adv. Drug Deliv. Rev.* **56**, 173–184 (2004).
7. C. G. Cameron, M. S. Freund, Electrolytic actuators: Alternative, high-performance, material-based devices. *Proc. Natl. Acad. Sci. U.S.A.* **99**, 7827–7831 (2002).
8. N. T. Nguyen, X. Huang, T. K. Chuan, MEMS-micropumps: A review. *J. Fluids Eng.* **124**, 384–392 (2002).

Avila et al.
Modeling programmable drug delivery in bioelectronics with electrochemical actuation

9. F. Amirouche, Y. Zhou, T. Johnson, Current micropump technologies and their biomedical applications. *Microsyst. Technol.* **15**, 647–666 (2009).

10. D. J. Laser, J. G. Santiago, A review of micropumps. *J. Micromech. Microeng.* **14**, R35–R64 (2004).

11. H. Gensler, R. Sheybani, P. Y. Li, R. L. Mann, E. Meng, An implantable MEMS micropump system for drug delivery in small animals. *Biomed. Microdevices* **14**, 483–496 (2012).

12. A. M. Cobo, H. M. Tu, R. Sheybani, E. Meng, "Characterization of a wireless implantable infusion micropump for small animal research under simulated in vivo conditions" in *Proceedings of the 2014 IEEE Biomedical Circuits and Systems Conference (BioCAS) Proceedings*, Lausanne, Switzerland, 22–24 October 2014; pp. 348–351.

13. F. L. Trull, B. A. Rich, More regulation of rodents. *Science* **284**, 1463 (1999).

14. D. B. Young, T. E. Jackson, D. H. Pearce, A. C. Guyton, A portable infusion pump for use on large laboratory animals. *IEEE Trans. Biomed. Eng.* **24**, 543–545 (1977).

15. Y. Zhang *et al.*, Battery-free, lightweight, injectable microsystem for in vivo wireless pharmacology and optogenetics. *Proc. Natl. Acad. Sci. U.S.A.* **116**, 21427–21437 (2019).

16. Y. Zhang *et al.*, Battery-free, fully implantable optofluidic cuff system for wireless optogenetic and pharmacological neuromodulation of peripheral nerves. *Sci. Adv.* **5**, eaaw5296 (2019).

17. S. Spieth *et al.*, An intra-cerebral drug delivery system for freely moving animals. *Biomed. Microdevices* **14**, 799–809 (2012).

18. J. W. Jeong *et al.*, Wireless optofluidic systems for programmable in vivo pharmacology and optogenetics. *Cell* **162**, 662–674 (2015).

19. M. Staples, Microchips and controlled-release drug reservoirs. *Wiley Interdiscip. Rev. Nanomed. Nanobiotechnol.* **2**, 400–417 (2010).

20. D. J. H. Tng, R. Hu, P. Song, I. Roy, K. T. Yong, Approaches and challenges of engineering implantable microelectromechanical systems (MEMS) drug delivery systems for in vitro and in vivo applications. *Micromachines (Basel)* **3**, 615–631 (2012).

21. P. Y. Li *et al.*, An electrochemical intraocular drug delivery device. *Sens. Actuators A Phys.* **143**, 41–48 (2008).

22. C. Pang, Y. C. Tai, J. W. Burdick, R. A. Andersen, Electrolysis-based diaphragm actuators. *Nanotechnology* **17**, S64–S68 (2006).

23. C. Neagu, H. Jansen, H. Gardeniers, M. Elwenspoek, Electrolysis of water: An actuation principle for MEMS with a big opportunity. *Mechatronics* **10**, 571–581 (2000).

24. C. R. Neagu, J. G. E. Gardeniers, M. Elwenspoek, J. J. Kelly, An electrochemical microactuator: Principle and first results. *J. Microelectromech. Syst.* **5**, 2–9 (1996).

25. T. Stanczyk, B. Ilic, P. J. Hesketh, J. G. Boyd IV, Microfabricated electrochemical actuator for large displacements. *J. Microelectromech. Syst.* **9**, 314–320 (2000).

26. S. Böhm, W. Olthuis, P. Bergveld, An integrated micromachined electrochemical pump and dosing system. *Biomed. Microdevices* **1**, 121–130 (1999).

27. P. Y. Li, R. Sheybani, C. A. Gutierrez, J. T. W. Kuo, E. Meng, A parylene bellows electrochemical actuator. *J. Microelectromech. Syst.* **19**, 215–228 (2010).

28. A. Kabata *et al.*, Prototype micropump for insulin administration based on electrochemical bubble formation. *J. Pharm. Sci.* **97**, 5037–5045 (2008).

29. A. Cobo, R. Sheybani, H. Tu, E. Meng, A wireless implantable micropump for chronic drug infusion against cancer. *Sens. Actuators A Phys.* **239**, 18–25 (2016).

30. H. Gensler *et al.*, "Implantable MEMS drug delivery device for cancer radiation reduction" in *IEEE 23rd International Conference on Micro Electro Mechanical Systems (MEMS)* (IEEE, Wanchai, Hong Kong, 2010), pp. 23–26.

31. J. Urquhart, J. W. Fara, K. L. Willis, Rate-controlled delivery systems in drug and hormone research. *Annu. Rev. Pharmacol. Toxicol.* **24**, 199–236 (1984).

32. M. W. Ashraf, S. Tayyaba, N. Afzulpurkar, Micro Electromechanical Systems (MEMS) based microfluidic devices for biomedical applications. *Int. J. Mol. Sci.* **12**, 3648–3704 (2011).

33. M. H. Smolensky, N. A. Peppas, Chronobiology, drug delivery, and chronotherapeutics. *Adv. Drug Deliv. Rev.* **59**, 828–851 (2007).

34. B. B. C. Youan, Chronopharmaceutics: Gimmick or clinically relevant approach to drug delivery? *J. Control. Release* **98**, 337–353 (2004).

35. D. E. Lee, S. A. Soper, W. Wang, Fabrication and mathematical analysis of an electrochemical microactuator (ECM) using electrodes coated with platinum nanoparticles. *Microsyst. Technol.* **16**, 381–390 (2010).

36. R. Sheybani, E. Meng, "High efficiency wireless electrochemical actuators: Design, fabrication and characterization by electrochemical impedance spectroscopy" in *Proc. IEEE Int. Conf. MEMS.* (IEEE, Cancun, Mexico, 2011), pp. 1233–1236.

37. D. J. Beebe, G. A. Mensing, G. M. Walker, Physics and applications of microfluidics in biology. *Annu. Rev. Biomed. Eng.* **4**, 261–286 (2002).

38. H. Bruus, *Theoretical Microfluidics* (Oxford University Press, 2009).

39. M. Mooney, A theory of large elastic deformation. *J. Appl. Phys.* **11**, 582–592 (1940).

40. R. S. Marlow, "A general first-invariant hyperelastic constitutive model" in *Constitutive Models for Rubber III*, J. Busfield, Ed. (AA Balkema Publishers, UK, 2003), pp. 157–160.

41. Dassault Systèmes, *Analysis User's Manual. Version 6.10, Dassault Systèmes Simulia, Inc.* (Dassault Systèmes Simulia, Inc., 2010).

42. S. Timoshenko, S. Woinowsky-Krieger, "Symmetrical bending of circular plates" in *Theory of Plates and Shells* (McGraw-Hill, New York, 1959), pp. 51–78.